
# Development of Wideband Transmitarray Antennas With Adaptive Bidirectional Beam Reconfigurability for mm-Wave IoT Applications

Mei, Peng; Pedersen, Gert Frølund; Zhang, Shuai

*Published in:*
IEEE Internet of Things Journal

*DOI (link to publication from Publisher):*
10.1109/JIOT.2025.3578055

*Publication date:*
2025

*Document Version*
Accepted author manuscript, peer reviewed version

# Development of Wideband Transmitarray Antennas with Adaptive Bidirectional Beam Reconfigurability for mm-Wave IoT Applications

Peng Mei, *Senior Member*, *IEEE*, Gert Frølund Pedersen, *Member*, *IEEE*, and Shuai Zhang, *Fellow, IEEE*

***Abstract*— This article proposes a scheme to enable wideband and beam-reconfigurable transmitarray (TA) antennas with flexible bidirectional beams for Internet of Things (IoT) applications. The proposed scheme primarily consists of a polarization-rotation-based (PR-based) phase-shifting surface (PSS), a dielectric lens, and a feed source. By leveraging distinct frequency responses of the PR-based PSS and dielectric lens to electromagnetic (EM) waves, the proposed scheme can achieve exceptional beam reconfigurability. To validate the scheme, a bidirectional beam-reconfigurable TA antenna is developed. By mechanically rotating the feed source to tune its polarization from *x*- to *y*-polarization, the beam of the developed TA antenna transitions from a single forward beam, through a bidirectional beam, and finally to a single rearward beam, all remaining the same polarization. Notably, when the feed source is rotated to be 45-deg polarization, the forward and rearward beams exhibit comparable gains. The gain variation of the forward/rearward beam approximately follows cos($\theta$), where $\theta$ is the rotation angle of the feed source. Simulated results reveal that the developed TA antenna works well from 24 GHz to 28.5 GHz, exhibiting robust continuous and adaptive bidirectional beam reconfigurability with sidelobe levels below -15 dB and cross-polarization levels below -20 dB. A prototype is characterized, where the measured results align well with the simulated ones. With versatile beam-steering capabilities, the developed TA antenna is well-suited for 5G millimeter-wave (mm-wave)-enabled IoT applications, such as smart transportation systems, dual-side railway/roadway communication networks, and tunnel-based communication infrastructures.**

***Index Terms* — Beam-reconfigurable, dielectric lens, polarization rotation, bidirectional beam, transmitarray antenna.**

## I. Introduction

With the increasingly complex electromagnetic (EM) environment and evolving application scenarios, advanced antenna solutions are essential to ensure reliable, efficient, and adaptable wireless communication systems, serving as the backbone in the realm of the Internet of Things (IoT) scenarios. Among the many antenna solutions, high gain and beam-reconfigurable antennas are particularly critical, especially in the millimeter-wave band, where free space path loss is significant. Millimeter-wave beam-reconfigurable antennas are capable of directing EM signals toward specific users, securing sufficient data capacity while effectively maintaining the link budget and enhancing overall communication performance [1]-[6].

Recent advancements have led to the development of millimeter-wave high-gain and beam-steerable antennas. Phased arrays are a classic solution to achieve high gain and beam steering, where each antenna element connects with an RF chain composed of phase shifters, power amplifiers, etc [7] – [9]. However, this solution suffers from high loss, high power consumption, etc, making it less suitable for energy-efficient IoT deployments. Reconfigurable reflectarray/ transmitarray antennas (RR/TAs) [10] – [21] have emerged as promising alternatives. RR/TAs are generally divided into two categories as per the control method. The electrical method involves loading PIN diodes on unit cells (UCs) [10] – [12] or using liquid crystal as the substrate [13], [14]. PIN-diode-loaded UCs achieve discrete phase states by switching the diodes ON or OFF, while the liquid-crystal-based UCs allow for continuous phase states by tuning the permittivity of the liquid crystal with applied voltage. The mechanical method, on the other hand, adjusts UC's rotation [15], [16], height [17], or uses multiple feed sources [18] – [21] to introduce the desired phase gradient for beam steering. Compared to the electrical method, the mechanical one is advantageous for energy-efficient IoT applications, as it reduces power consumption by eliminating the need for RF components.

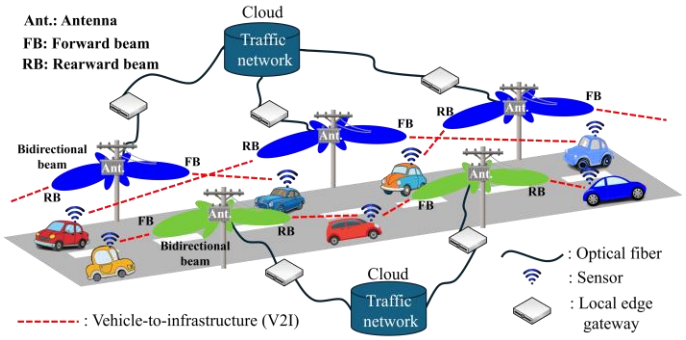


Fig.1. Demonstration of the line-of-sight (LOS) scenario of antennas with bidirectional beams for vehicle-to-infrastructure within the IoT framework.

This work was supported in part by DFF project 1 and in part by innovationsfonden project of DRONE. (*Corresponding author: Peng Mei*.)

The authors are with the Antennas, Propagation and Millimeter-Wave Systems Section, Department of Electronic Systems, Aalborg University, 9220 Aalborg, Denmark (e-mail: mei@es.aau.dk).

While most beam-steerable RR/TAs mentioned above focus on unidirectional radiation, recent efforts have developed antennas with high gain and bidirectional radiation capabilities [21] – [25]. For instance, the authors in [23] designed a low-profile and high-gain antenna with a bidirectional radiation beam by combining a folded TA antenna and a Fabry-Perot (FP) cavity antenna. However, the polarizations of the forward and rearward beams are orthogonal, which is a potential drawback in practical applications. The authors in [24] developed a hybrid TA with reconfigurable bidirectional beams, where the same polarizations for the forward and rearward beams are achieved. In this design, the authors built upon our previous work [26] to implement the five-layer polarization rotating metasurface that guarantees the same polarizations for the incoming and outgoing waves. However, the fabrication cost of five-layer polarization-rotating metasurfaces is rather high due to the lamination technology in the printed-circuit-board (PCB) manufacturing process.

In this article, we propose a similar yet economical and powerful scheme compared to [24]. By fully leveraging the distinct frequency responses of the polarization-rotation-based (PR-based) phase-shifting surface (PSS) and the dielectric lens to electromagnetic (EM) waves, the proposed scheme can achieve remarkable bidirectional beam reconfigurability. For proof of the scheme, a bidirectional beam-reconfigurable TA antenna is built with a 2-bit PR-based FSS, a 2-bit dielectric lens, and a multilayer stacked feed source for wideband operation. By mechanically rotating the feed source to tune its polarization from *x*- to *y*-polarization, the beam of the developed TA antenna transitions from a single forward beam gradually through a bidirectional beam and finally to a single rearward beam. Furthermore, the polarizations of all the beams always remain consistent due to the polarization-sensitive property of the PR-based PSS and the polarization-insensitive property of the dielectric lens. A prototype is fabricated and characterized. The measured results, aligning well with the simulated ones, show that the developed TA antenna works well from 24.0 to 28.5 GHz, exhibiting robust continuous and adaptive bidirectional beam reconfigurability. The measured sidelobe levels and cross-polarization levels of all the beams (i.e., single forward beam, bidirectional beam, and single rearward beam) are below -15 dB and -20 dB, respectively. The measured results also indicate that the gain variation of the forward/rearward beam approximately follows $\cos(\theta)$, where $\theta$ represents the rotation angle of the feed source.

With its exceptional beam-reconfigurable capabilities, the developed TA antenna is well-suited for 5G millimeter-wave-enabled IoT applications, particularly in dynamic and infrastructure-intensive environments such as smart transportation systems, dual-side railway/roadway communication networks, and tunnel-based communction infrastructures. For instance, an illustrative vehicle-to-infrastructure (V2I) within the IoT framework is envisioned and presented in Fig. 1. In this context, the developed TA antennas are strategically deployed on roadside infrastructures and support continuous and adaptive bidirectional beam coverage – labeled as forward beam (FB) and rearward beam (RB) – which can be dynamically configured to adjust the gain of the bidirectional beam, accommodating the traffic flow conditions (e.g., peak and off-peak hours). In such scenarios, rapid beam-switching is not a critical requirement. The forward beam establishes a high-gain link with sensors equipped on approaching vehicles, facilitating the efficient acquisition of key traffic information such as vehicle type, density, and status. This received data is firstly processed by the local edge gateways and subsequently is uploaded via high-speed optical fibers to the centralized traffic management network for broader analysis and network updates. Concurrently, the rearward beam maintains continued connectivity with departing vehicles, supporting functions like tracking vehicle speed, lane change monitoring, or route adherence verification for timely feedback to the centralized traffic network. This continuous and adaptive beam reconfigurability allows for more energy-efficient operation while maintaining robust and low-latency communications between edge infrastructures and vehicles. The novelty and key advantages of the developed TA antenna with adaptive and bidirectional beams are explicitly discussed in Section VI.

The outline of the article is organized as follows: Section II introduces the general scheme to enable bidirectional beam-reconfigurable TA antennas. Section III details the elements to implement PR-based PSS, dielectric lens, and wideband antenna. The TA antenna with continuous and adaptive bidirectional beam reconfigurability is developed in Section IV. Experimental verifications for the developed TA antenna are carried out in Section V. Section VI highlights and discusses the key features of the developed TA antenna. Some remarkable conclusions are drawn in Section VII.

## II. The Scheme For Bidirectional Beam Reconfigurability

Without loss of generality, Fig. 2 displays the proposed scheme for bidirectional beam reconfigurability. It consists of upper and lower phase-shifting surfaces and a feed source that could be either embedded within the lower PSS or suspended between the upper and lower PSSs.

The working principle of the proposed scheme is explicitly explained in the following. We assume that the feed source is linearly polarized, and its polarization can be varied with its axially mechanical rotation. Fig. 2(d) illustrates a front view of the feed source with a 45-degree polarization. The EM waves radiating from the feed source can always be decomposed into two orthogonal components (i.e., *x*-polarized and *y*-polarized EM waves). The upper PSS exhibits specific electromagnetic properties that only let *x*-polarized incoming EM waves pass through it with the outgoing EM waves *y*-polarized as illustrated in Fig. 2(b), while *y*-polarized incoming EM waves get reflected. By contrast, the lower PSS is polarization-insensitive, allowing arbitrarily polarized incoming EM waves to propagate through it while preserving the same polarization for the outgoing EM waves as shown in Fig. 2(c).

The proposed scheme, illustrated in Fig. 2(a), features a high degree of freedom in beam reconfigurability. Three notable beams are explained here:

1). When the feed source is rotated to be purely *x*-polarized, the proposed scheme can only generate a single forward beam.

2). A single rearward beam is solely obtained when the feed source is rotated to pure *y*-polarization.

3). A bidirectional beam with comparable gains for the forward and rearward beams can be achieved when the feed source is rotated to be 45-degree polarization (The same aperture sizes and the appropriate separation are assumed).

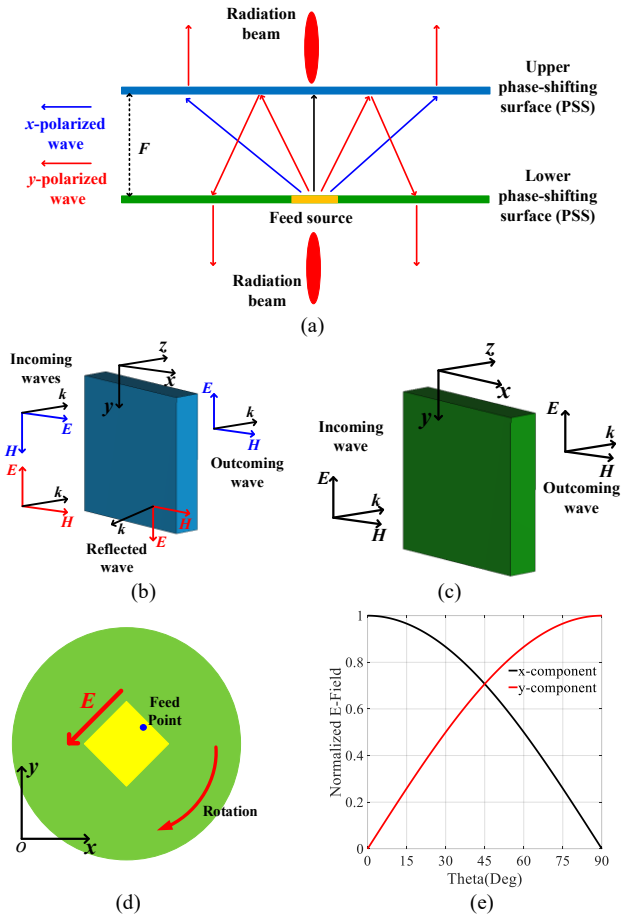


Fig. 2. The proposed scheme to achieve bidirectional beam reconfigurability. (a). The whole scheme. (b). The EM responses of the upper PSS. (c). The EM responses of the lower PSS. (d). The feed source is oriented at 45-degree polarization. (e). The decomposed normalized E-field in *x* and *y*-direction with different rotation angles of the feed source.

As a result, continuous and adaptive bidirectional beam reconfigurability is expected to be achieved. Specifically, by mechanically rotating the feed source to make its polarization convert from *x*- to *y*-polarization, where the decomposed normalized E-field in *x*- and *y*-direction with different rotation angles of the feed source is plotted in Fig. 2(e), the beam will transition from a single forward beam gradually through a bidirectional beam and finally to a single rearward beam.

It is also found that the performance of the single forward beam, bidirectional beam, and single rearward beam enabled by the proposed scheme can be flexibly manipulated. It could be achieved either through joint control of the air separation between the upper and lower PSSs, or independent regulation of their aperture sizes. Additionally, the bandwidth of the proposed scheme could be broad if the upper and lower PSSs, along with the feed sources are properly designed with wide bandwidth, as will be demonstrated in this article.

## III. Implementation of the Elements for PR-based PSS, Dielectric Lens, and Wideband Antenna

In this section, we aim to design elements to implement the upper and lower PSSs, and wideband linearly-polarized feed source, which will be utilized to build the TA antenna with continuous and adaptive bidirectional beam reconfigurability.

### *A. The element design for the upper phase-shifting surface*

The polarization-rotation-based (PR-based) element is a promising candidate to generate the electromagnetic responses required by the upper PSS as depicted in Fig.1. Such an element is therefore proposed accordingly with its geometry shown in Fig. 3. It consists of three metal layers, two of which are orthogonal-oriented polarizers, and the middle layer is a square ring with slits. The substrates (colored with Green) used here are Roger 4003C with a dielectric constant of 3.55 and loss tangent of 0.0027. The thicknesses are $t_1$ = 0.508 mm and $t_2$= 0.305 mm, respectively. The bonding film (colored with Aqua) used to glue two substrates is Rogers 4450F with a dielectric constant of 3.52, a loss tangent of 0.0027, and a thickness of 0.202 mm. Such a PR-based element inherently enables a 1-bit transmission phase (i.e., 0 and π) by simply rotating the middle metal layer 90 degrees, without altering the element's dimensions.

The transmission phase shift of a PR-based element is typically obtained by tuning the specific dimensions of the middle metal layer [27], [28]. Take the element illustrated in Fig. 3 for example, the transmission phase shift is usually obtained by tuning the widths of the slits. However, it is found that resizing the slits shifts the operating frequency and leads to a narrow bandwidth of the element, which is undesirable for wideband designs. To address it, the effective strategy proposed in [26] is adopted here to broaden the bandwidth of the PR-based element. We properly configure two elements so that they can not only provide a similar wide bandwidth but also achieve a 2-bit transmission phase quantization for simplification of the design. The periodicity of the PR-based element is typically in the range of 0.2λ – 0.3λ based on well-established design practices [24], [26], [27]. The actual periodicity should be fine-tuned to achieve the desired amplitude and phase responses. Here, the periodicity of the proposed element is optimized and set to 3 mm, corresponding to 0.25λ (λ is the wavelength in free space at 25 GHz), to make it work well within the frequency range of interest.

The elements are simulated and evaluated with CST Studio Suite, with periodic boundary conditions (PBC) applied to the element to emulate an infinite surface. The S-parameters of the two elements are plotted in Fig. 4, indicating that the proposed two elements maintain high transmission efficiencies with insertion loss below 0.8 dB and offer a stable 2-bit

transmission phase from 22 to 30 GHz. The key dimensions of the two elements are summarized and tabulated in Tab. I.

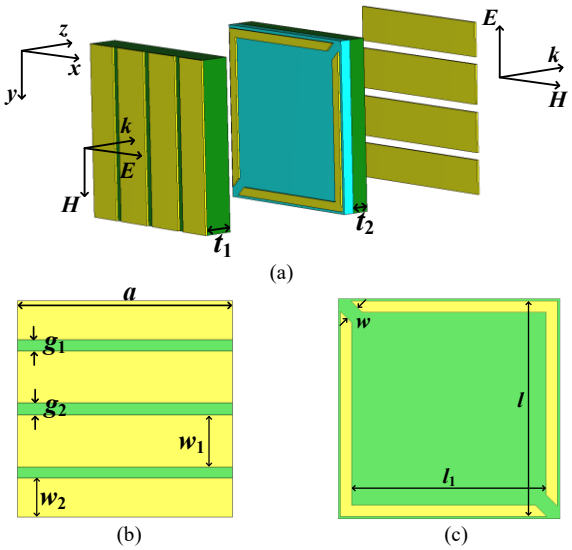


Fig. 3. The geometry of the element to implement the upper PSS. (a). The expanded perspective view of the element. (b). The front view of the element. (c). The front view of the middle layer. ($a$ = 3 mm, $g_1$ = 0.13 mm, $g_2$ = 0.14 mm, $w_1$ = 0.7 mm, $w_2$ = 0.6 mm, $w$ = 0.2 mm)

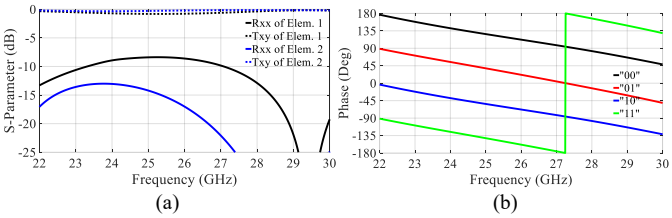


Fig. 4. The frequency responses of the elements to implement the upper PSS. (a). Amplitude of S-parameter. (b). Transmission phases of the two elements.

Tab. I. The key dimensions of the two elements to achieve the desired phases

| | ($l$, $l_1$) | Phase |
|---|---|---|
| Elem. 1 | (2.1 mm, 1.8 mm) | -180, 0 |
| Elem. 2 | (2.9 mm, 2.6 mm) | -90, 90 |

### *B. The element design for lower phase-shifting surface*

To pair the wide bandwidth of the elements that are employed to build the upper PSS, the dielectric-based element capable of providing the desired electromagnetic responses is utilized to construct the lower PSS. The geometry of the dielectric-based element is shown in Fig. 5, where it is an air-perforated dielectric stub with a periodicity of 0.25λ (λ is the wavelength in free space at 25 GHz). The material of the dielectric is Acrylonitrile Butadiene Styrene (ABS) with a dielectric constant of 2.55 and loss tangent of 0.02 at the frequency band of interest, which is compatible with available 3D printers. By tuning the width ($p$) of the air hollow or the height ($h$) of the element, the dielectric-based element achieves different transmission phases, and the transmission loss is varied accordingly. To balance the height, transmission phases, losses of the elements, and the printing accuracy of the 3D printer available in our lab, four elements are properly configured to permit wide bandwidth while simultaneously achieving a 2-bit transmission phase quantization.

The S-parameters of the four elements are simulated using CST Studio Suite with the same boundary conditions as the PR-based element, and then plotted in Fig. 6. It is observed that the four elements keep high transmission coefficients (insertion loss below 1.5 dB) and offer a 2-bit transmission phase simultaneously from 20 to 30 GHz. The key dimensions of the four elements are listed in Tab. II. Notably, when $p$ = 3.0 mm, the element is effectively degenerated to pure air. Conversely, the element is a pure dielectric stub with no air hollow when $p$ = 0 mm.

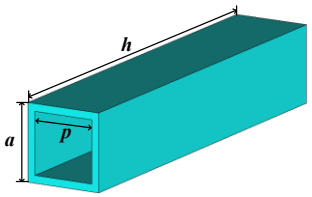


Fig. 5. The geometry of the dielectric-based element to implement the lower PSS. ($a$ = 3 mm, $h$ = 15 mm)

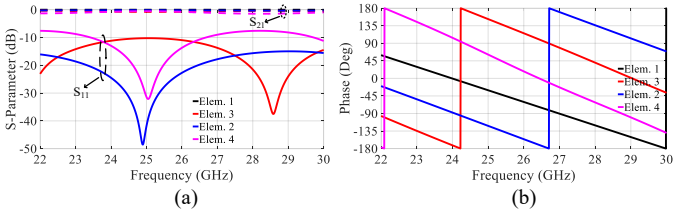


Fig. 6. The frequency responses of the four elements to implement the lower PSS. (a). Amplitude of S-parameter. (b). Transmission phase.

Tab. II. The key dimensions of the four dielectric-based elements to achieve the desired phases

| | $p$ | Phase |
|---|---|---|
| Elem. 1 | 3.00 mm | 90 |
| Elem. 2 | 2.41 mm | 0 |
| Elem. 3 | 1.71 mm | -90 |
| Elem. 4 | 0 mm | -180 |

### *C. Wideband feed source*

A wideband antenna is designed in this subsection to serve as the feed source. For brevity, we adopt the same multilayer configuration as the PR-based element to design the patch antenna. The geometry of the patch antenna is displayed in Fig. 7. To permit the same $x$ and $y$-component decomposed from the patch antenna when its polarization is 45 degrees, the driven and stacked patches are shaped to be square as illustrated in Figs. 7(a) and (b). Furthermore, the patch antenna is reshaped to be circular as shown in Fig. 7(d) to guarantee smooth mechanical rotation of the feed source. The radius of the circular shape is set to 7 mm, occupying approximately 5 × 5 elements of the lower PSS in total.

The dimensions of the driven and stacked patches are optimized to make the patch antenna operate at the frequency band of interest. Fig. 8(a) displays the simulated reflection coefficient of the patch antenna, where the reflection

coefficient below -10 dB from 24 to 28.5 GHz is obtained. The radiation patterns of the patch antenna are also examined at 26 GHz on *xoz*- and *yoz*-plane as illustrated in Fig. 8(b), where identical radiation patterns are obtained that are consistent with its 3D radiation pattern as depicted in Fig. 7(e).

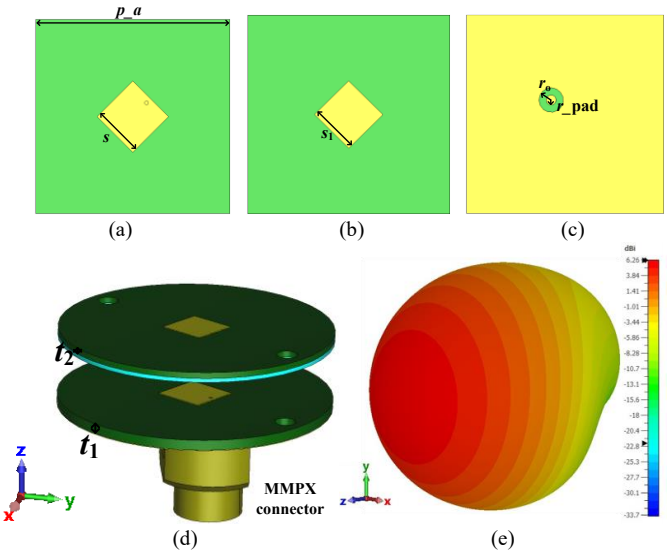


Fig. 7. The geometry of the patch antenna. (a). The front view of the driven patch. (b). The front view of the stacked patch. (c). The back view. (d). The expanded perspective view of the 45-degree-polarized patch antenna. (e). The simulated 3D radiation pattern of the patch antenna at 26 GHz. ($p\_a$ = 10 mm, $s$ = 2.6 mm, $s_1$ = 2.4 mm, $r_o$ = 0.615 mm, $r$_pad = 0.25 mm.)

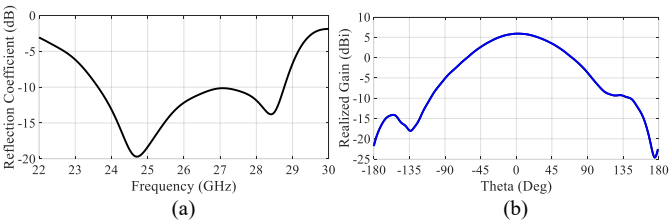


Fig. 8. The simulated results of the patch antenna. (a). Reflection coefficient. (b). Radiation pattern on the *xoz*- and *yoz*-plane at 26 GHz.

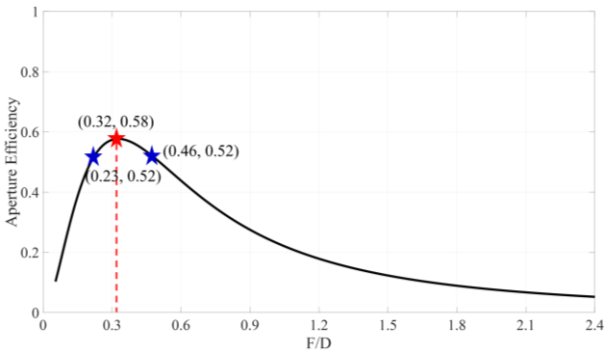


Fig. 9. The relationship between aperture efficiency and different F/D ratios of a TA antenna at 26 GHz.

## IV. Implementation of Continuous and Adaptive Bidirectional Beam-Reconfigurable TA Antenna

Section III has designed the elements to build the upper and lower PSSs as well as the wideband patch antenna, which will be utilized in this Section to develop the TA antenna with continuous and adaptive bidirectional beam reconfigurability.

As it is known to all, the performance (i.e., realized gain, aperture efficiency, etc.) of a TA antenna is closely related to the ratio of focal distance to aperture size ($F/D$) and radiation pattern of the feed source [29], where $F$ is the distance from the phase center of the feed source to the geometrical center of the PSS, and $D$ is the length of the PSS. Generally, a larger D correlates with a higher realized gain. For demonstration, we assume the aperture size of 93 mm × 93 mm to balance the total simulation time of the developed TA antenna and its realized gain. It should be noted that the aperture size can be scaled down and up depending on the specific application requirements. Based on this aperture size, we plot the aperture efficiency of a TA antenna with different $F/D$ as shown in Fig. 9, where the radiation pattern of the patch antenna designed in Section III at 26 GHz is adopted.

As seen in Fig. 9, a maximum aperture efficiency is theoretically obtained when the $F/D$ ratio is 0.32. Referring to Fig. 2(a), the EM waves responsible for generating the rearward beam travel twice the propagation path for the forward beam. As a result, a proper $F/D$ ratio of 0.23 can be selected according to Fig. 9 to permit comparable gains (i.e., aperture efficiency) for the forward and rearward beams. It should be noted, however, that the curve plotted in Fig. 9 is derived under ideal assumptions. In practice, hardware limitations such as losses of elements, non-isotropic radiation patterns of elements, mutual couplings among elements, the finite size of the upper PSS, etc. should be considered. After some optimizations, $F$ is finally finalized at 25 mm, corresponding to a $F/D$ ratio of 0.268.

With the defined configuration (i.e., the aperture size of 93 mm × 93 mm and $F$ = 25 mm), the continuous phase distribution on the observation plane [step (1) in Fig. 10], where the PR-based PSS is positioned, is subsequently simulated at 26 GHz when the polarization of the feed source is purely *x*-polarized and then plotted as depicted in Fig. 11(a). It is noted that the vertical distance between the phase center of the feed source and the geometric center of the observation plane is $F$ which is equal to 25 mm. We then utilize 2-bit phase quantization to approximate the continuous phase distribution, as illustrated in Fig. 11(b). Based on the quantized phase distribution, the PR-based PSS is therefore built using the designed elements shown in Fig. 3.

To construct the dielectric lens, we need to know the phase distribution on the observation plane [step (2) in Fig. 10] where the dielectric lens will be positioned. We rotate the feed source 90 degrees to make the polarization *y*-polarized so that *y*-polarized EM waves emanating from the feed source get reflected when illuminating the built PR-based PSS. Then, the phase distribution on the plane is simulated and depicted as illustrated in Fig. 12(a), and its corresponding 2-bit quantized phase quantization is plotted in Fig. 12(b) and is utilized to build the dielectric lens with the elements designed in Fig. 5. At this stage, the TA antenna with continuous and adaptive bidirectional beam reconfigurability has been developed, as

shown in step (3) of Fig. 10.

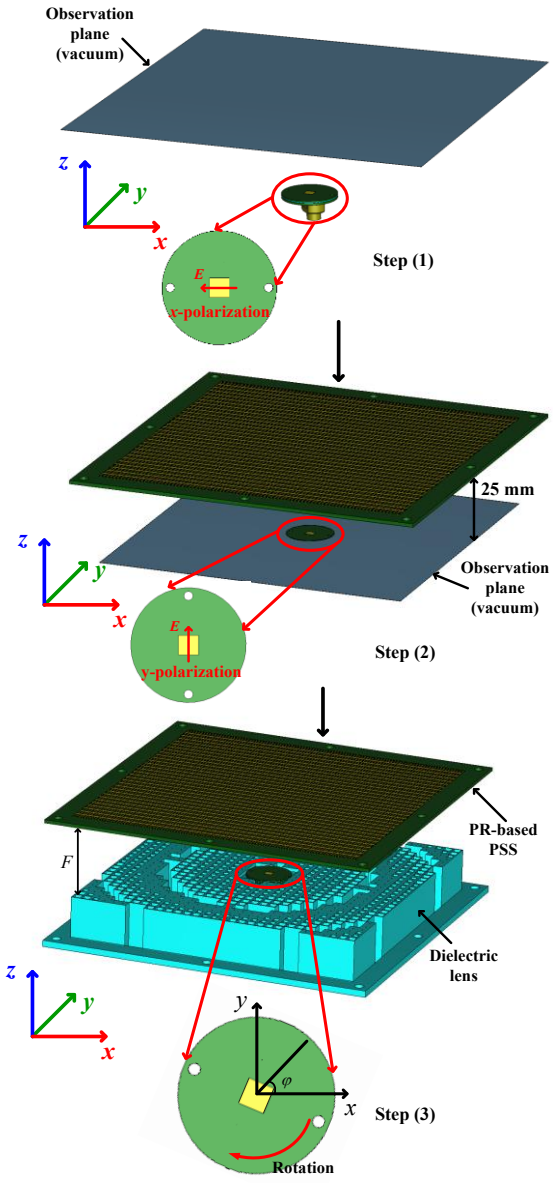


Fig. 10. The evolutional steps to implement the TA antenna with continuous and adaptive bidirectional beam reconfigurability from a single forward beam gradually through a bidirectional beam, and finally to a single rearward beam.

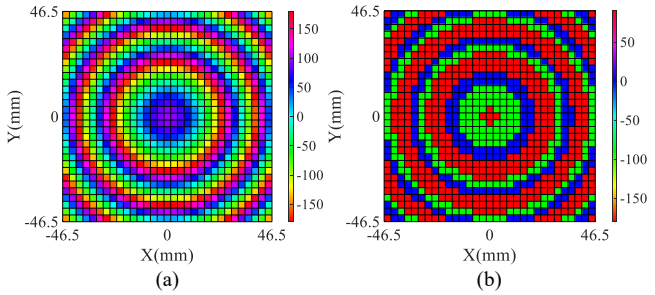


Fig. 11. The phase distribution on the plane of the upper PR-based PSS at 26 GHz. (a). The continuous phase distribution. (b). The corresponding 2-bit quantized phase distribution.

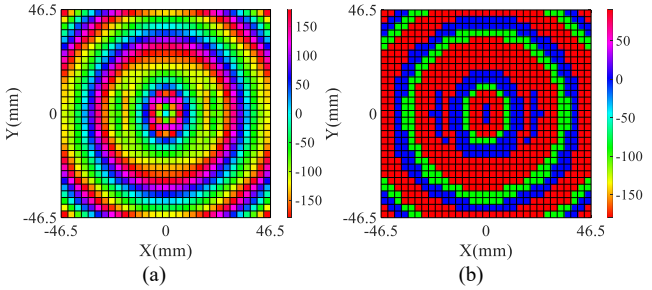


Fig. 12. The phase distribution on the plane of the lower dielectric lens at 26 GHz. (a). The continuous phase distribution. (b). The corresponding 2-bit quantized phase distribution.

The radiation patterns of the developed TA antenna are simulated when the feed source is rotated with different angles from 0 deg to 90 deg. As can be seen in Fig. 13, the developed TA antenna can generate a single forward beam when the feed source is purely *x*-polarized. As the feed source gradually rotates toward *y*-polarization, the single forward beam gradually transitions into a bidirectional beam since the radiating field can be decomposed into *x*- and *y*-component, and eventually to a single rearward beam when the feed source is rotated to be purely *y*-polarized. Notably, although the beam reconfigurability of the developed TA antenna is achieved by mechanically rotating the feed source (the polarization of the feed source is varied during the rotation), the polarizations of all beams – namely, the single forward beam, the bidirectional beams, and the single rearward beam – always remain consistent. This consistency is attributed to the polarization-sensitive property of the PR-based PSS and the polarization-insensitive property of the dielectric lens.

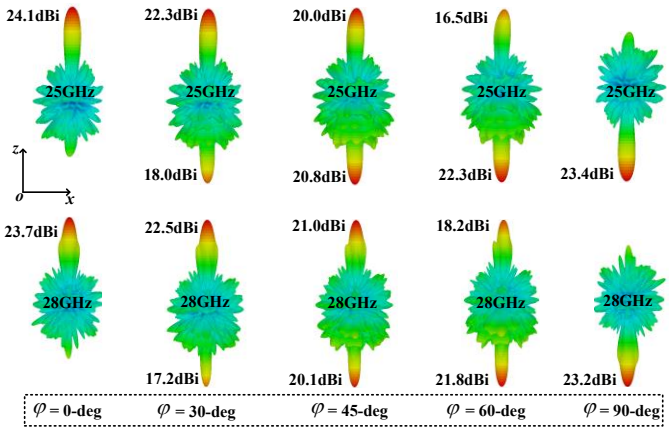


Fig. 13. The 3D radiation pattern at 25 GHz and 28 GHz, respectively, when the feed source rotates with different angles.

## V. Experimental Verifications

To validate the full-wave simulations described above, the developed TA antenna is fabricated and characterized in this Section. The PR-based PSS and wideband patch antenna are fabricated with lamination technology in the PCB processing, while the dielectric lens is printed with our available 3D printer (RAISE3D Pro2). The prototype is shown in Fig. 14.

The patch antenna is embedded within the dielectric lens, and the dielectric lens and PR-based PSS are separated by metallic pillars with a height of 25 mm. The $S_{11}$ of the developed TA antenna is first measured with a power network analyzer (PNA) with different rotation angles of the feed source. It is found that measured $S_{11}$ remains consistent with different rotation angles. For brevity, the measured $S_{11}$ of the developed TA antenna with the feed source *x*-polarized is plotted in Fig. 15, alongside the corresponding simulated result for comparison. The measured $S_{11}$ closely aligns with the simulated one, which is below -10 dB from 24 to 28.5 GHz.

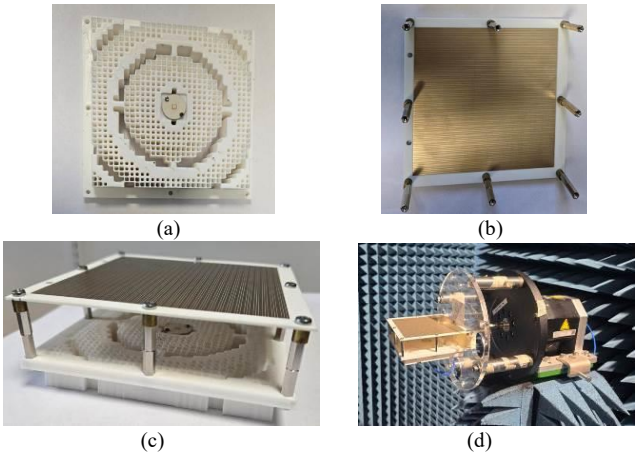


Fig. 14. The prototype and measurement environment of the developed TA antenna. (a). The dielectric lens. (b). PR-based PSS. (c). The assembled TA antenna. (d). The measurement setup in the anechoic chamber.

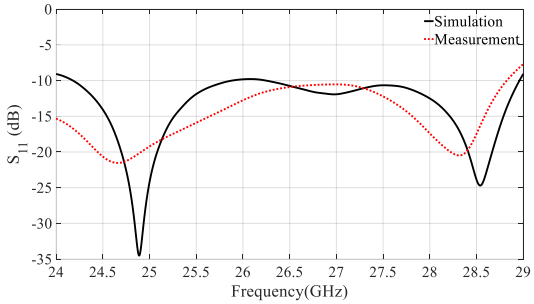


Fig. 15. The measured and simulated reflection coefficient of the developed TA antenna when the feed source is *x*-polarized.

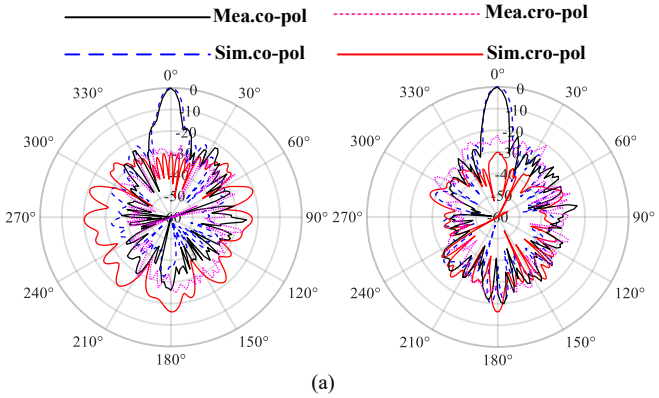


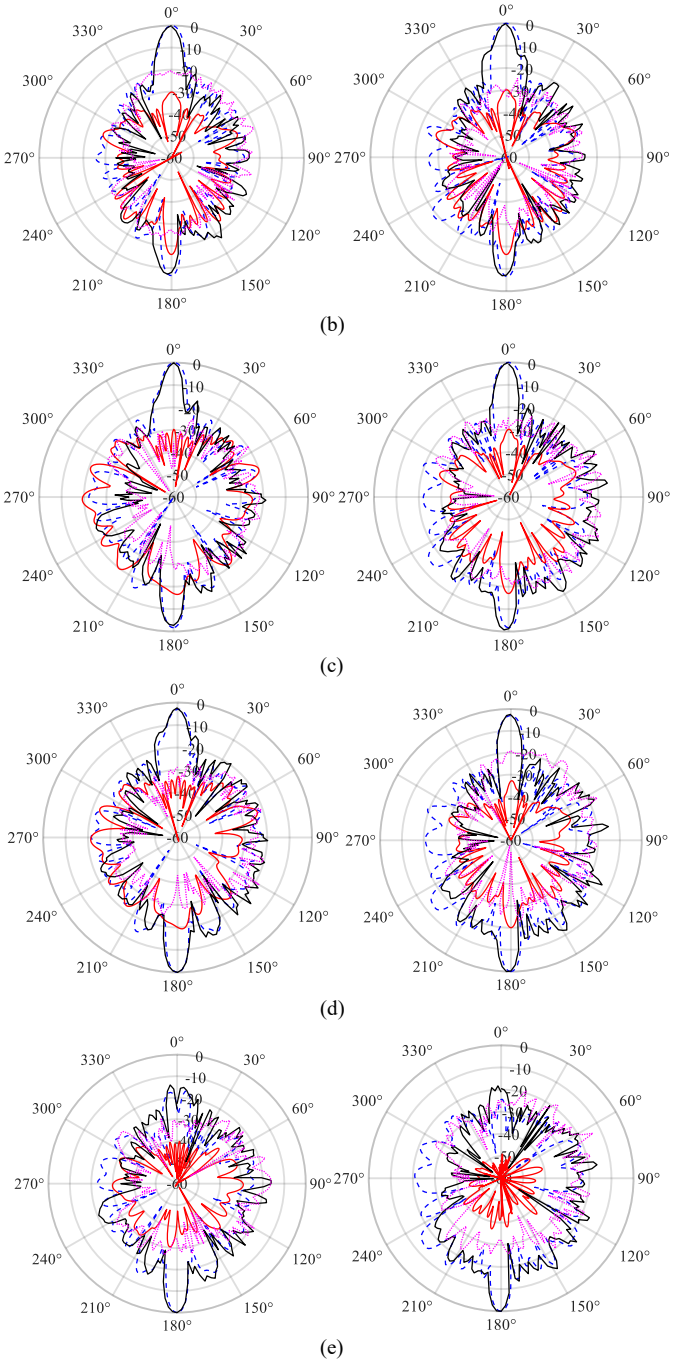


Fig. 16. Measured and simulated radiation patterns of the proposed TA antenna at 26 GHz. (a). 0°. (b). 30°. (c). 45°. (d). 60°. (e). 90°. (Left: phi = 0°, Right: phi = 90°, co-pol: co-polarization, cro-pol: cross-polarization).

The radiation patterns of the developed TA antenna are also measured in the anechoic chamber at Aalborg University. To demonstrate its continuous and adaptive bidirectional beam reconfigurability, the feed source is manually rotated during measurements, which can be improved by equipping the feed source with a mini motor for automated rotation control in the future. Here, we only present the measured radiation patterns of the developed TA antenna at 26 GHz with different rotation angles of the feed source for brevity. Fig. 16 displays the measured radiation patterns when the feed source is rotated to 0°, 30°, 45°, 60°, and 90°, alongside the corresponding

simulated results for comparison. As observed from Fig. 16, the beam of the developed TA antenna transitions from a single forward beam, gradually through a bidirectional beam, and finally to a single rearward beam. Specifically, a single forward and beam is obtained when the feed source is rotated to 0º and 90º, respectively, while in between these angles, a bidirectional beam with distinct gains for forward and rearward beams is achieved, validating the continuous and adaptive bidirectional beam reconfigurability. Additionally, it is also observed that the sidelobe levels of all the beams are below -15 dB, and the measured cross-polarization levels are also below -20 dB for all the beams. The measured results agree well with the simulated ones, verifying the effectiveness of the developed TA antenna.

In addition, the realized gains of the forward and rearward beams are measured at different rotation angles (i.e., 0º, 30º, 45º, 60º, and 90º) of the feed source and are also compared with the simulations. As can be seen in Fig. 17, the measured realized gains of the forward beam are slightly lower than the simulated results, whereas the measured realized gains of the rearward beam exhibit a more significant gain reduction than the simulated counterparts. In addition to the measurement tolerance, the discrepancy is also attributed to fabrication tolerances. The PR-based PSS, responsible for generating the forward beam, can be well manufactured with lamination technology to offer precise phase shifts, which has a limited impact on the performance of the forward beam. In contrast, the dielectric lens contributes to the rearward beam. Printing tolerances such as surface roughness, uniform infilling ratio, etc. affect the precision of phase shifts of the dielectric lens, leading to gain reductions. It is also observed from Fig. 17 that the gain variation at different rotation angles approximately follows cos($\theta$), where $\theta$ is the rotation angle. Additionally, according to Fig. 17, the measured realized gains for the single forward and rearward beams reach up to 24.0 dBi and 21.8 dBi, respectively. The aperture efficiency of the developed TA antenna can be evaluated with the measured realized gain, using the following formula:

$$\eta = \frac{G\lambda^2}{4\pi S} \quad (1)$$

where $G$ is the realized gain, $\lambda$ is the wavelength in free space at the frequency of interest, and $S$ is the physical area of the phase-shifting surface. Using Eq. (1), the calculated aperture efficiencies at 26 GHz are 33% for the forward beam and 22.1% for the rearward beam.

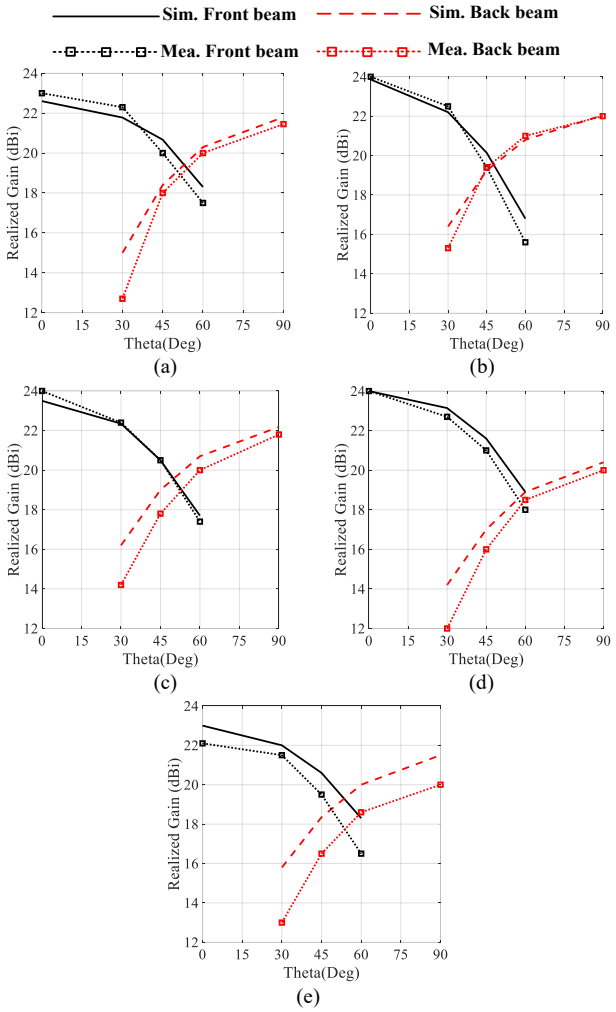


Fig. 17. Measured and simulated gains of the forward and rearward beams at different rotation angles of the feed source. (a). 24 GHz. (b). 25 GHz (c). 26 GHz (d). 27 GHz. (e). 28 GHz.

Tab. III. Comparison of the developed TA antenna based on the proposed scheme with the state-of-the-art bidirectional beams

| Ref | Frequency ($\lambda_0$, GHz) | Feed source | Gain bandwidth | Beam-control method | Beam states | Forward/rearward beam gain (dBi) | Aperture efficiency (%) | Overall profile | Complexity/ Cost |
|---|---|---|---|---|---|---|---|---|---|
| [21] (2023) | 9.5 | Horn | 19.5% (3.0 dB) | PIN diodes | $+z$, $-z$, $\pm z$ | 21.4/21.0 | 19.2/17.3 | *4.43$\lambda_0$ | High |
| [24] (2024) | 9.75 | Patch | 15.4% (3.0 dB) | PIN diodes | $+z$, $-z$, $\pm z$ | 23.6/23.1 | 13.3/11.9 | 7.24$\lambda_0$ | High |
| [25] (2019) | 5.35 | Horn | 19.0% (1.0 dB) | PIN diodes | $\pm z$ | 17.2/15.4 | #8.2/5.4 | *7.14$\lambda_0$ | High |
| **This work** | **26** | **Patch** | **17.1% (2.0 dB)** | **Mechanical rotation** | **Continuous from $+z$ to $-z$ (vice versa)** | **24/21.8** | **33/22.1** | **3.46$\lambda_0$** | **Low** |

*: the profile of the horn is excluded. #: the aperture efficiency is calculated with simultaneous forward and rearward beams.

## VI. Discussion

This section evaluates the performance of the developed TA antenna based on the proposed scheme and benchmarks it against state-of-the-art with similar bidirectional beams. As seen in Tab. III, the developed TA antenna demonstrates superior performance in terms of gain bandwidth, beam-reconfigurable capability, aperture efficiency, total profile, and implementation complexity/cost. It is observed that Refs. [21] and [25] also exhibit good gain bandwidth, which is primarily attributed to their similar configurations – both employing a horn to illuminate an expensive reconfigurable surface loaded with PIN diodes. In general, the bandwidth of a horn is much wider than that of a patch antenna. As a result, the bandwidth of the developed TA antenna in our work is mainly constrained by the patch antenna which serves as the feed source. Since Ref. [24] has a similar configuration to ours, we highlight the key features of the developed TA antenna in comparison to [24]:

a). ***Enhanced Beam Reconfigurability***: The developed TA antenna supports continuous and adaptive bidirectional beam reconfigurability, smoothly transitioning from a single forward beam, gradually through a bidirectional beam, and finally to a single rearward beam, achieved by mechanically rotating the feed source. In contrast, the hybrid TA antenna in [24] offers only three discrete beams: a single forward beam, a bidirectional beam with comparable gains for the forward and rearward beams, and a single rearward beam, which are achieved by PIN-diodes-enabled polarization-reconfigurable feed source. As a result, the beam-reconfigurable capability of the developed TA antenna is more advanced and competitive, making it better suited for a wider range of IoT scenarios.

b). ***Wider Bandwidth Performance***: The developed TA antenna exhibits enhanced bandwidth performance, attributed to the wideband design of the PR-based PSS, dielectric lens, and multilayer stacked patch antenna. Additionally, the exclusion of active components, such as loading PIN diodes on the feed source to electrically manipulate its polarization [24], minimizes parasitic effects and losses, thereby further improving the overall bandwidth and system efficiency.

c). ***Cost-Effective Fabrication***: The fabrication cost of the developed TA antenna is significantly lower than that of the design presented in [24]. In PCB manufacturing using lamination technology, the fabrication cost tends to increase exponentially with the number of layers approximately. Therefore, the five-layer metasurface in [24] incurs considerably higher fabrication costs compared to the three-layer PSS employed in the developed TA antenna. This cost reduction makes the developed TA antenna more feasible for large-scale productions and real-world deployments.

It is observed that the dielectric lens in this article has a relatively high profile. The high profile, on the one hand, slightly degrades the performance of the dielectric lens due to strong oblique incidence effects, on the other hand, it could be a potential drawback that limits the practical application of the developed TA antenna in some space-constrained scenarios. However, the overall profile can be significantly reduced by using a high-permittivity material for printing the dielectric lens. Specifically, employing ABS1500 – a high-permittivity material with a dielectric constant of 14.0, compatible with commercial 3D printers – could reduce the overall profile by approximately 1/3.

## VII. Conclusion

In summary, this article presents a similar yet cost-effective and powerful scheme to enable TA antenna with bidirectional beams. Based on the proposed scheme, a wideband TA antenna with continuous and adaptive bidirectional beam reconfigurability has been developed and characterized. By mechanically rotating the feed source to tune its polarization, the beam of the developed TA antenna transitions smoothly from a single forward beam, gradually through a bidirectional beam, and finally to a single rearward beam. Experimental results align with the simulated ones, verifying the effectiveness and performance of the proposed scheme and developed TA antenna. With its enhanced beam reconfigurability, wider bandwidth performance, and cost-effective fabrication, the developed TA antenna stands out as a competitive solution in comparison to the current state-of-the-art and similar work.

While the current study has demonstrated the feasibility and performance of the proposed TA antenna under controlled laboratory conditions, which is a preliminary yet essential step toward real-world IoT applications, practical IoT deployment scenarios typically involve dynamic and complex electromagnetic environments. In real-world settings, factors such as mobility, multipath propagation, Doppler shifts, and environmental variability (e.g., buildings, vehicles, and foliage) can affect antenna performance. It should be mentioned here, however, since the developed TA antenna exhibits high gain at the mm-wave band, the impact of the multipath effects is expected to be minimal in line-of-sight (LOS) scenarios. Nevertheless, as part of future work, we aim to integrate the developed TA antenna into a V2I test platform to evaluate its robustness and adaptability under realistic environments, aiming to further validate the developed TA antenna in practical IoT applications from a system-level perspective, such as smart transportation systems, dual-side railway or roadway communication networks, and tunnel-based communication infrastructures.

## References

[1].J. Xu, K. Wang, Y. Lu, L. Mei, Y. Wang, C. Ding, and M. Yu, "A 2-bit beam-steering coding array with high beam pointing accuracy and side lobe level for wide-angle beam scanning", *IEEE Internet Things J.*, DOI: 10.1109/JIOT.2025.3552118.

[2].S. Pan, M. Liu, M. Xu, S. Zhu, L. Bian, and G. Li, "A low-profile programmable beam scanning holographic array antenna without phase shifters", *IEEE Internet Things J.*, vol. 9, no. 11, pp. 8838 – 8851, June 2022.

[3].Z. Wang, and Y. Dong, "Novel pattern reconfigurable epsilon-near-zero (ENZ) antenna for intelligent IoT communication applications", *IEEE Internet Things J.*, vol. 11, no. 12, pp. 22364 – 22375, June 2024.

[4].L. Wang, et al., "Multibeam metasurface antenna enabled by orbital angular momentum demultiplexing feeding for IoT communications", *IEEE Internet Things J*., vol. 10, no. 18, pp. 16169 – 16182, Sep 2023.
[5].S. Gaya, A. Hamza, O. Sokunbi, S. Sheikh, and H. Attia, "Electronically switchable frequency and pattern reconfigurable segmented patch antenna for internet of vehicles", *IEEE Internet Things J*., vol. 11, no. 10, pp. 17840 – 17851, May 2024.
[6].R. Alwashishi, M. Ali, G. Elzwawi, and T. Denidni, "Beam-switching antenna using reconfigurable intelligent frequency selective surfaces for internet of things applications", *IEEE Internet Things J*., vol. 11, no. 3, pp. 4152 – 4162, Feb 2024.
[7]. D. Paker, and D. Zimmermann, "Phased arrays – part I: theory and architectures", *IEEE Trans. Microwave Theory Tech*., vol. 50, no. 3, pp. 678 – 687, Mar 2002.
[8]. D. Paker, and D. Zimmermann, "Phased arrays – part II: implementations, applications, and future trends", *IEEE Trans. Microwave Theory Tech*., vol. 50, no. 3, pp. 688 – 698, Mar 2002.
[9].T. Latha, G. Ram, G. Arun Kumar, and M. Chakravarthy, "Review on ultra-wideband phased array antennas", *IEEE Access*, vol. 9, pp. 129742 – 129755. 2021.
[10]. Q. Luo, S. Gao, W. Li, M. Sobhy, I. Bakaimi, and C. H. Kees de Groot, "Multibeam dual-circularly polarized reflectarray for connected and autonomous vehicles", *IEEE Trans. Veh. Technol*., vol. 68, no. 4, pp. 3574 – 3585, Apr 2019.
[11]. B. Xiang, X. Dai, and K. M. Luk, "A wideband low-cost reconfigurable reflectarray antenna with 1-bit resolution", *IEEE Trans. Antennas Propag*., vol. 70, no. 9, pp. 7439 – 7447, Sep 2022.
[12]. H. Yang, F. Yang, S. Xu, Y. Mao, M. Li, X. Cao, and J. Guo, "A 1-bit 10 x 10 reconfigurable reflectarray antenna: design, optimization, and experiment", *IEEE Trans. Antennas Propag*., vol. 64, no. 6, pp. 2246 – 2254, June 2016.
[13]. R. Guirada, G. Perez-Palomino, P. Rosa, E. Carrasco, and X. Quintana, "Electronically reconfigurable reflectarray antenna based on single-layer liquid crystal with independent dual-polarization control", *IEEE Trans. Antennas Propag*., vol. 72, no. 7, pp. 5626 – 5636, July 2024.
[14]. P. Aghabeyki, Y. Cai, G. Deng, Z. Tan, and S. Zhang, "A dual-polarized reconfigurable reflectarray with a thin liquid crystal layer and 2-D beam steering", *IEEE Trans. Antennas Propag*., vol. 71, no. 4, pp. 3282 – 3293, Apr 2023.
[15]. X. Yang, S. Xu, F. Yang, M. Li, Y. Hou, S. Jiang, and L. Liu, "A broadband high-efficiency reconfigurable reflectarray antenna using mechanically rotational elements", *IEEE Trans. Antennas Propag*., vol. 65, no. 8, pp. 3959 – 3966, Aug 2017.
[16]. P. Mei, S. Zhang, and G. F. Pedersen, "A low-cost, high-efficiency and full metal reflectarray antenna with mechanically 2-D beam-steerable capabilities for 5G applications", *IEEE Trans. Antennas Propag*., vol. 68, no. 10, pp. 6997 – 7006, Oct 2020.
[17]. M. Teng, S. Yu, N. Kou, Z. Ding, and Z. Zhang, "Mechanical beam steering array antenna with tunable height", *IEEE Antennas Wireless Propag. Lett*., vol. 21, no. 11, pp. 2293 – 2297, Nov. 2022.
[18]. M. Jiang, Z. Chen, Y. Zhang, W. Hong, and X. Xuan, "Metamaterial-based thin planar lens antenna for spatial beamforming and multibeam massive MIMO", *IEEE Trans. Antennas Propag*., vol. 65, no. 2, pp. 464 – 472, Feb 2017.
[19]. P. Mei, G. F. Pedersen, and S. Zhang, "Performance improvement of mechanically beam-steerable transmitarray antennas by using offset unifocal phase symmetry", *IEEE Trans. Antennas Propag*., vol. 71, no. 1, pp. 1129 – 1134, Jan 2023.
[20]. J. Yang, Y. Shen, L. Wang, H. Meng, W. Dou, and S. Hu, "2-D scannable 40-GHz folded reflectarray fed by SIW slot antenna in a single-layered PCB", *IEEE Trans. Microwave Theory Tech*., vol. 66, no. 6, pp. 3129 – 3135, June 2018.
[21]. H. Yu, P. Li, J. Su, Z. Li, S. Xu, and F. Yang, "Reconfigurable bidirectional beam-steering aperture with transmitarray, reflectarray, and transmit-reflect-array modes switching", *IEEE Trans. Antennas Propag*., vol. 71, no. 1, pp. 581 – 595, Jan 2023.
[22]. S. Liu, X. Lin, Y. Yan, and Y. Fan, "Generation of high-gain and bidirectional transmit-reflect-array antenna with asymmetric beams using spare-array method", *IEEE Trans. Antennas Propag*., vol. 69, no. 9, pp. 6087 – 6092, Sep 2021.
[23]. R. Gao, M. Yang, Q. Guo, and W. He, "A low-profile and high-gain antenna with bidirectional beams enabled by integrating folded transmitarray and Fabry-Perot Cavity", *IEEE Trans. Antennas Propag*., vol. 72, no. 8, pp. 6209 – 6218, Aug 2024.
[24]. Q. Fan, Y. Liu, C. Gu, L. Zeng, W. Cheng, H. Zhang, and S. Gao, "Multibeam hybrid transmitarray based on polarization rotating metasurface with reconfigurable bidirectional radiation", *IEEE Trans. Antennas Propag*., vol. 72, no. 9, pp. 6992 – 7004, Sep 2024.
[25]. M. Wang, S. Xu, F. Yang, and M. Li, "A 1-bit bidirectional reconfigurable transmit-reflect-array using a single-layer slot element with PIN diodes", *IEEE Trans. Antennas Propag*., vol. 67, no. 9, pp. 6205 – 6210, Sep 2019.
[26]. P. Mei, G. F. Pedersen, and S. Zhang, "A broadband and FSS-based transmitarray antenna for 5G millimeter-wave applications", *IEEE Antennas Wireless Propag. Lett*., vol. 20, no. 1, pp. 103 – 107, Jan. 2021.
[27]. M. Honari, K. Mavrakakis, H. Luyen, J. Booske, and N. Behdad, "A dual-band transmitarray antenn aemploying ultra-thin, polarization-rotating spatial phase shifter", *IEEE Trans. Antennas Propag*., vol. 70, no. 11, pp. 11132 – 11137, Nov 2022.
[28]. P. Feng, S. Qu, and S. Yang, "Octave bandwdith transmitarrays with a flat gain", *IEEE Trans. Antennas Propag*., vol. 66, no. 10, pp. 5231 – 5238, Oct 2018.
[29]. A. Yu, F. Yang, A. Z. Elsherbeni, J. Huang, and Y. Rahmat-Samii, "Aperture efficiency analysis of reflectarray antennas", *Microwave Opt Technol. Lett.*, vol. 52, no. 2, pp. 364 – 372, Feb. 2010.

**Peng Mei** (Senior Member, IEEE) is currently working as a full professor at Huazhong University of Science and Technology, Wuhan, China. He received his B.Eng. and M. Eng. (with the highest honor) degrees in electromagnetic fields and microwave technology from the University of Electronic Science and Technology of China (UESTC), China, in 2015 and 2018, respectively, and got his Ph.D. degree in wireless communications from Aalborg University, Denmark, in 2021. Dr. Mei finished his postdoctoral training at the Antennas, Propagation, and Millimeter-Wave Systems (AMPS) section, Aalborg University, Denmark, in 2023, and then worked as assistant professor at the APMS section from 2023 to 2025. His current research interests include periodic structures, metasurfaces, beam-steerable and 3D printing antennas, transmitarray/reflectarray antennas, and reconfigurable intelligent surfaces. He has authored/co-authored around 35 notch-top journal papers, 23 conference proceedings, and one PCT patent that has been sold to industrial partner.

Dr. Mei was a recipient of the Excellent Master Thesis from the Chinese Institute of Electronics (CIE) in 2019, and served as a best paper competition co-chair of the 2023 International Workshop on Antenna Technology, held at Aalborg, Denmark, served as the chief guest editor of the special issue "Advanced Massive MIMO Antenna Arrays, Metasurfaces, and Reconfigurable Intelligent Surfaces for Sensing, Localization, and Wireless Communications" launched by Sensors in 2022, and the chief guest editor of the special section "Recent Advances on Absorbers/Rasorbers and Their Applications on Antennas and EMC" launched by IEEE Open Journal of Antennas and Propagation in 2023. He was invited to give a talk at the 2024 International Workshop on Antenna Technology held in Japan, has been listed in the World Top 2% Scientists in Year 2023 and 2024 for two consecutive years, and a recipient of top reviewers of IEEE Transactions on Antennas and Propagation from 2022 to 2024 for three consecutive years. Dr. Mei has been selected as 2025 IEEE Antennas and Propagation Society Young Professional Ambassador and is the associate editor for Sensors.

**Gert Frølund Pedersen** (Member, IEEE) was born in 1965. He received the B.Sc. degree (Hons.) in electrical engineering from the College of Technology, Dublin, Ireland, in 1991, and the M.Sc. degree in electrical engineering and the Ph.D. degree from Aalborg University, Aalborg, Denmark, in 1993 and 2003, respectively.

Since 1993, he has been with Aalborg University, where he is currently a Full Professor. He was also the Head of the Doctoral School on Wireless Communication. He has also involved as a consultant for the development of more than 100 antennas for mobile terminals, including the first internal antenna for mobile phones in 1994 with the lowest specific absorption rate (SAR), first internal triple-band antennas in

1998 with low SAR and high TRP and TIS, and lately various multiantenna systems rated as the most efficient on the market. He has involved most of the time with joint university and industry projects and has received more than U.S. $12 M in direct research funding. He is the Project Leader of the SAFE Project with a total budget of U.S. $8 M investigating tunable front end, including tunable antennas for the future multiband mobile phones. He has been one of the pioneers in establishing over-the-air (OTA) measurement systems. The measurement technique is now well established for mobile terminals with single antenna, and he was chairing the various COST groups (swg2.2 of COST 259, 273, 2100, and now ICT1004) with liaison to 3GPP for OTA test of MIMO terminals. He is also deeply involved in MIMO OTA measurement. He has authored or coauthored more than 300 peer-reviewed papers and holds 49 patents. His research has focused on radio communication for mobile terminals, especially small antennas, diversity systems, and propagation and biological effects.

**Shuai Zhang** (Fellow, IEEE) received the B.E. degree from the University of Electronic Science and Technology of China, Chengdu, China, in 2007 and the Ph.D. degree in electromagnetic engineering from the Royal Institute of Technology (KTH), Stockholm, Sweden, in 2013. In 2014, he joined Aalborg University, Denmark, where he is currently a Full Professor and the Head of Antenna Research Group. In 2010 and 2011, he was a Visiting Researcher at Lund University, Sweden and at Sony Mobile Communications AB, Sweden, respectively. He was also an external antenna specialist at Bang & Olufsen, Denmark from 2016-2017. He has supervised/co-supervised 10 Postdocs and 18 PhD students. He has coauthored over 140 articles in well-reputed international journals and over 17 US or WO patents. His citations in Scopus are over 6000 with H index of 40. His current research interests include: millimeter-wave antennas for cellular communications, bio-electromagnetics, metasurfaces, CubeSat antennas, Massive MIMO antennas, wireless sensors, and RFID antennas.

He is the Associate Editor for IEEE Antennas and Wireless Propagation Letters; and IET Microwaves, Antennas and Propagation. He is the General Co-Chair for iWAT2023 at Aalborg, Denmark, and the TPC or meta reviewer for several top IEEE conferences. He is the recipient of “IEEE Antennas and Propagation Society Young Professional Ambassador” in 2022, where he gives presentation for different IEEE Chapters on Antennas for Mobile Communications. He has also been intensively invited to international conference and industry to give keynote/plenary speech and presentations. From 2024, he has been the European Association on Antennas and Propagation (EurAAP) Regional Delegate.